

Empirical beam hardening and ring artifact correction for x-ray grating interferometry (EBHC-GI)

Brandon J. Nelson^{a)}

Graduate Program in Biomedical Engineering and Physiology, Mayo Clinic Graduate School of Biomedical Sciences, Rochester, MN 55905, USA

Department of Radiology, Mayo Clinic, Rochester, MN 55905, USA

Shuai Leng, Elisabeth R. Shanblatt and Cynthia H. McCollough

Department of Radiology, Mayo Clinic, Rochester, MN 55905, USA

Thomas Koenig

Graduate Program in Biomedical Engineering and Physiology, Mayo Clinic Graduate School of Biomedical Sciences, Rochester, MN 55905, USA

Ziehm Imaging, Lina-Ammon-Str. 10, Nuremberg 90471, Germany

(Received 4 August 2020; revised 3 November 2020; accepted for publication 8 December 2020; published 10 January 2021)

Purpose: Talbot-Lau grating interferometry enables the use of polychromatic x-ray sources, extending the range of potential applications amenable to phase contrast imaging. However, these sources introduce beam hardening effects not only from the samples but also from the gratings. As a result, grating inhomogeneities due to manufacturing imperfections can cause spectral nonuniformity artifacts when used with polychromatic sources. Consequently, the different energy dependencies of absorption, phase, and visibility contrasts impose challenges that so far have limited the achievable image quality. The purpose of this work was to develop and validate a correction strategy for grating-based x-ray imaging that accounts for beam hardening generated from both the imaged object and the gratings.

Methods: The proposed two-variable polynomial expansion strategy was inspired by work performed to address beam hardening from a primary modulator. To account for the multicontrast nature of grating interferometry, this approach was extended to each contrast to obtain three sets of correction coefficients, which were determined empirically from a calibration scan. The method's feasibility was demonstrated using a tabletop Talbot-Lau grating interferometer micro-computed tomography (CT) system using CT acquisitions of a water sample and a silicon sample, representing low and high atomic number materials. Spectral artifacts such as cupping and ring artifacts were quantified using mean squared error (MSE) from the beam-hardening-free target image and standard deviation within a reconstructed image of the sample. Finally, the model developed using the water sample was applied to a fixated murine lung sample to demonstrate robustness for similar materials.

Results: The water sample's absorption CT image was most impacted by spectral artifacts, but following correction to decrease ring artifacts, an 80% reduction in MSE and 57% reduction in standard deviation was observed. The silicon sample created severe artifacts in all contrasts, but following correction, MSE was reduced by 94% in absorption, 96% in phase, and 90% in visibility images. These improvements were due to the removal of ring artifacts for all contrasts and reduced cupping in absorption and phase images and reduced capping in visibility images. When the water calibration coefficients were applied to the lung sample, ring artifacts most prominent in the absorption contrast were eliminated.

Conclusions: The described method, which was developed to remove artifacts in absorption, phase, and normalized visibility micro-CT images due to beam hardening in the system gratings and imaged object, reduced the MSE by up to 96%. The method depends on calibrations that can be performed on any system and does not require detailed knowledge of the x-ray spectrum, detector energy response, grating attenuation properties and imperfections, or the geometry and composition of the imaged object. © 2020 American Association of Physicists in Medicine [<https://doi.org/10.1002/mp.14672>]

Key words: beam hardening, grating interferometry, image quality, phase contrast, ring artifacts, Talbot-Lau

1. INTRODUCTION

X-ray phase and normalized visibility are the two novel contrasts accessible via grating interferometry that have gained attention due to their claimed improved contrasts in soft tissues and porous materials, respectively, when compared to traditional absorption radiography.^{1–3} The use of Talbot-Lau grating interferometry⁴ broadens potential preclinical and clinical applications of simultaneously measuring x-ray absorption, differential phase, and normalized visibility by using polychromatic sources with greater tube output.⁵ This increased flux is particularly important for reducing scan times in grating-based methods that lose x-ray intensity due to grating absorption. However, the use of polychromatic sources comes at the cost of biasing quantitative measurements by introducing spectral artifacts including beam hardening.⁶ While beam hardening is an established area of study in x-ray absorption imaging, differences in grating-based systems and derived contrasts contribute additional challenges, motivating the development of specialized grating-based corrections.

Beam hardening is a consequence of the energy dependence of x-ray interactions particularly in higher atomic number materials. In medical x rays, energy-dependent absorption is proportional to $\frac{1}{E}$, where E is the photon energy.⁷ In samples of finite thickness, this causes polychromatic spectra to harden as lower energy x rays are preferentially attenuated. The remaining higher energy photons interact less and yield underestimated and inhomogeneous absorption measurements. Similar effects exist for differential phase and normalized visibility contrast mechanisms in polychromatic grating-based experiments.⁸ The degree of bias in phase measurements differs from that of absorption due to the different physical contrast mechanisms⁹ and the different energy dependencies, which have been reported to be between $\frac{1}{E}$ and $\frac{1}{E^2}$ for phase.^{10,11} In addition, while normalized visibility is sensitive to unresolvable microstructures, it is also influenced by beam hardening.¹² Previous studies have shown normalized visibility to be correlated with absorption and phase contrasts when using polychromatic spectra.¹³ This suggests that the energy dependence of normalized visibility is also influenced by energy dependencies of absorption and phase. Therefore, despite presenting artifacts having a similar appearance, beam hardening correction schemes developed for standard absorption imaging systems cannot be directly applied to grating-based techniques because each contrast has a unique energy dependence and effective energy for a given system.^{9,11} This also suggests that contrast-specific corrections applied following phase retrieval are more effective than a single correction applied to the phase step data prior to phase retrieval. Additionally, gratings with translucent lamellae, a possible result of manufacturing errors,¹⁴ have been shown to further harden the beam.⁹ Given that grating transmission can vary over its area this can result in spectral nonuniformities as photons passing through different regions experience varying degrees of hardening.¹⁵ Thus a suitable correction scheme for grating interferometry must account for

both the beam hardening from the sample as well as the spectral artifacts from the gratings.

A range of grating-based beam hardening correction strategies have been developed that address many of these challenges. Early corrections used specialized calibration phantoms to appropriately scale each contrast projection to match expected values for the given phantom geometry and composition.¹¹ Analytical methods overcome the need for phantom calibration scans but require detailed system knowledge of the source spectra and detector response, while making assumptions on spectral responses of the sample and gratings.¹⁰ One solution developed to compensate for spectral artifacts from primary modulators lessens these assumptions by using iterative methods to estimate both the spectra and the effective modulator thickness at each detector pixel.¹⁵ Applied to grating interferometry such an approach would have to be expanded to estimate the effective thicknesses and spectral responses of all three gratings.

These corrections have largely corrected beam hardening artifacts caused by the object being imaged; however, there remain additional challenges from grating-induced beam hardening that have not yet been adequately resolved. This additional source of beam hardening can originate from any grating with partial transmission or nonideal phase modulation in their lamellae, and this biases all three contrasts.⁹ One solution could be to design gratings with taller lamellae to further reduce transmission, but this comes at the cost of reducing absorption and visibility contrast-to-noise ratios.¹⁴ Furthermore, partial transmission may be unavoidable in higher energy applications due to limitations in manufacturing gratings of sufficiently high aspect ratios.¹⁴

Dealing with beam hardening artifacts from gratings is uniquely challenging because they are spatially heterogeneous due to nonuniform lamellae thickness across the grating area resulting in spectral nonuniformity. In a grating interferometer, depicted schematically in Fig. 1(a), this variation in lamellae thickness translates into locally varying levels of absorption, phase, and visibility. This can be visualized in the uncorrected projections of a reference scan directly after standard Fourier processing,¹⁶ which we define here as $a_{0,r}, \phi_{1,r}$, and $V_{1,r}$ for the attenuation, differential phase, and normalized visibility contrasts, respectively. These uncorrected projections, shown in Fig. 1(b), show the underlying grating structures and are used to produce the corrected absorption, differential phase, and normalized visibility projections. The visible vertical and horizontal structures can originate from a variety of steps in the grating fabrication process and demonstrate the challenges of designing gratings with higher aspect ratios.¹⁴ Due to the nonlinear nature of beam hardening, some of these local variations are not completely removed from projections corrected using conventional flat-field methods once an object has been inserted into the beam. Thus, a correction is needed that accounts for beam hardening induced by both the sample and the gratings that also can be applied to each contrast mechanism: absorption, differential phase, and normalized visibility. Additionally, because grating inhomogeneities cannot be easily

modeled or known *a priori*, a successful correction method will require an empirical component.

The purpose of this work was to develop and validate such a correction strategy for grating-based x-ray imaging that accounts for beam hardening generated from both the imaged object and the gratings in all three contrasts. Experimental results using the proposed method are reported for data acquired using a water sample and a silicon sample that exhibited more severe beam hardening artifacts. Generalizability is then shown by applying the calibration coefficients obtained for a water sample to micro-CT data of a murine lung sample. Finally, we discuss the implications of this work for obtaining multicontrast information with polychromatic sources.

2. MATERIALS AND METHODS

2.A. Contrast-specific polynomial corrections

Polynomial corrections are an empirical prereconstruction beam hardening correction technique for conventional (absorption) x-ray imaging of objects dominated by a single material¹⁵ that map polychromatic projections q to monochromatic projections p . Empirical cupping correction (ECC)¹⁷ is one such polynomial correction that assumes this mapping to be of the form:

$$p = \sum_{i=0}^N c_i q^i, \quad (1)$$

for an N degree polynomial. Due to the linearity of the Radon transform (denoted by R), the $N+1$ correction coefficients c_i can be found in image space by minimizing for \mathbf{c}

$$\mathbf{c} = \operatorname{argmin}_{\mathbf{c}} \int d^3 r w(\mathbf{r}) \left(\sum_{i=0}^N c_i f_i(\mathbf{r}) - t(\mathbf{r}) \right). \quad (2)$$

Here $f_i(\mathbf{r}) = R^{-1}(q^i)$ are CT images reconstructed from projections q^i , $t(\mathbf{r})$ is the target image free of artifacts representing the vector of voxels \mathbf{r} , and $w(\mathbf{r})$ is a binary mask used to exclude region boundaries sensitive to partial volume effects.

Empirical cupping correction with a primary modulator (ECCP)¹⁸ is an extension of ECC developed to remove spatially dependent beam hardening artifacts generated by a primary modulator. This is accomplished by adding a variable M representing projections of the system's primary modulator such that Eq. (1) becomes

$$p = \sum_{i,j} c_{i,j} q^i M^j. \quad (3)$$

Similar to Eq. (2), coefficients $c_{i,j}$ are solved for in image space by minimizing

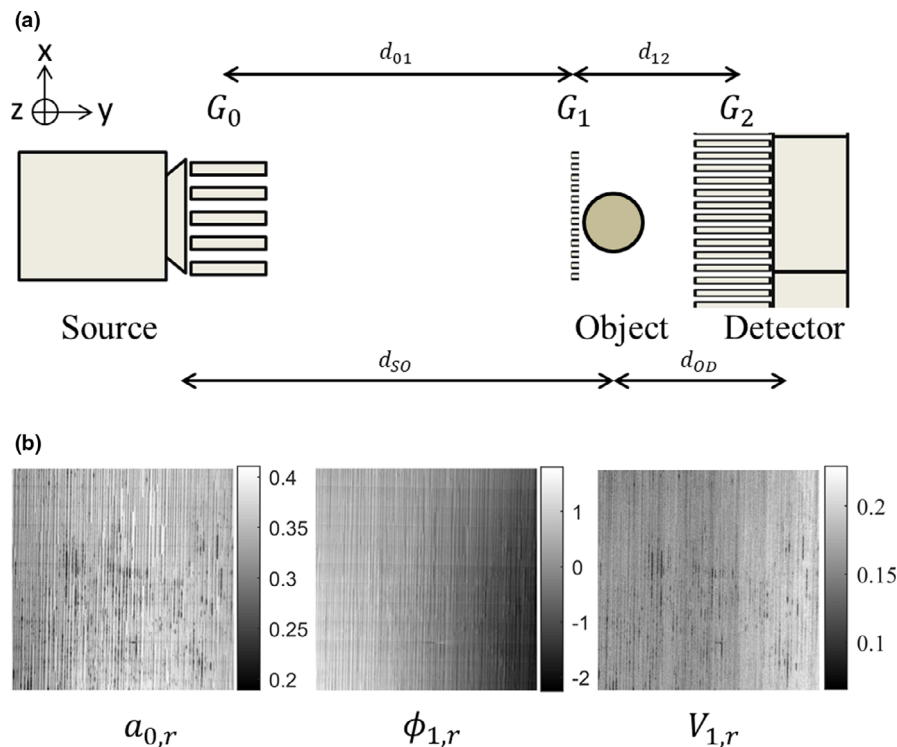


FIG. 1. Talbot-Lau grating interferometer (a). The source grating G_0 spatially modulates x rays from a source with a large focal spot. G_1 produces a downstream Talbot carpet sensitive to phase shifts induced by samples present within the beam path. G_2 matches the period of the Talbot interference pattern at its location, allowing the sampling of the high frequency interference pattern with large detector apertures using phase stepping or Fourier retrieval techniques. Distances d between gratings are noted at the top with distances between the source, object, and detector shown below. (b) Uncorrected projections of the reference scan directly after Fourier processing show underlying grating structure viewed in all three contrasts. [Color figure can be viewed at wileyonlinelibrary.com]

$$\mathbf{c} = \operatorname{argmin}_{\mathbf{c}} \int d^3r w(\mathbf{r}) \left(\sum_{i,j} c_{i,j} f_{i,j}(\mathbf{r}) - t(\mathbf{r}) \right), \quad (4)$$

with $f_{i,j}(\mathbf{r}) = R^{-1}(q^i M^j)$ being the reconstructed images following elementwise multiplication of projections q and primary modulator projections M raised to varying powers i and j . Specifically, the modulator projections are a reference air scan generated as $M = -\ln\left(\frac{I_0}{I_r}\right)$, where I_0 denotes the x-ray intensity with only the modulator present, while I_r is the intensity measured without any modulator or sample.

One approach to extending ECCP to grating interferometry would be to apply Eq. (3–4) directly to the phase stepping data to get a single set of correction coefficients. However, in preliminary work we found this to be not as effective as direct correction on each individual contrast. This is consistent with other studies that demonstrated that each contrast has a distinct system effective energy, suggesting a single compensation technique applied equally to all contrasts may not be as effective as specific compensations for each.^{8,9,11} That is why in this work we demonstrate how ECCP can be adapted for use in grating interferometry by applying the two-variable polynomial correction to each contrast, a technique we call empirical beam hardening correction for grating interferometry (EBHC-GI). Specifically, Eq. (3) and (4) become

$$p_k = \sum_{i,j} c_{k,i,j} q^i M^j, \quad (5)$$

$$\mathbf{c}_k = \arg \min_{\mathbf{c}_k} \int d^3r w_k(\mathbf{r}) \left(\sum_{i,j} c_{k,i,j} f_{k,i,j}(\mathbf{r}) - t_k(\mathbf{r}) \right), \quad (6)$$

where subscript k represents the different contrasts, $k = A$ for absorption, $\Delta\phi$ for differential phase, and V for normalized visibility. Now in Eq. (6), $f_{k,i,j}$ represents the reconstructed monomial projections $f_{k,i,j}(\mathbf{r}) = R^{-1}(q_k^i M_k^j)$. Correction coefficients $c_{k,i,j}$ are determined separately for each contrast k in the image domain. Like ECCP, $t_k(\mathbf{r})$ is found by applying Otsu's method¹⁹ or a similar automatic binary segmentation technique to the original reconstructed image for each contrast k . For the absorption and phase contrast channels, all values within each segmented region to be corrected are replaced with the median value within that region to approximate the desired beam-hardening-free value. By taking the median, large fluctuations from ring artifacts do not strongly influence the desired template value; however, severe cupping may still underestimate the true value to some degree. In the case of the visibility contrast channel, the beam-hardening-free template assumes no contrast in homogenous regions, thus their constant value is set equal to that of air. An additional step for prereconstruction linearization techniques is to record the minimum and maximum calibration values along with the correction coefficients. Then, when applying the correction technique only projection values that fall within the calibration range are updated to avoid spurious changes.¹⁷ EBHC-GI follows a similar practice of recording this calibration range for each set of contrast coefficients.

EBHC-GI deviates from ECCP again in its choice of spatial modulating term M . In the originally described ECCP method [Eq. (3)], the term M is an absorption projection of the primary modulator, acquired with no sample in the beam line, describing the spatial dependence of spectral artifacts induced by the primary modulator. However, in EBHC-GI the term M_k represents the influence of all three gratings for each image contrast k . In a cone-beam imaging system, the ring artifacts from gratings can vary substantially between slices. This variation is recorded in measurements of M_k for a given system. While in Eq. (5) the same correction coefficients c_k are mapped equally to all pixels, it is M_k that modulates the local ring artifact correction for each contrast.

In determining M_k , extrapolating ECCP to each contrast suggests using each contrast k 's reference air scan, $a_{0,r}, \phi_{1,r}$ and $V_{1,r}$ (see Section 2.C). Normalized visibility could be an exception as previous investigations have found polychromatic measurements of normalized visibility to correlate with absorption and phase contrast measurements in a system and material dependent manner.¹³ This suggests that grating spectral artifacts in absorption and differential phase projections can contaminate normalized visibility projections. Thus the absorption or phase reference image could be a better descriptor of these grating-related beam hardening artifacts in the normalized visibility channel if this effect was strong enough for a given system and material. This correlation of artifacts between contrasts was experimentally investigated using our Talbot-Lau grating interferometer micro-CT system where we empirically determined M_V for the normalized visibility contrast (see Section 2.D).

2.B. Sample preparation

Three samples were evaluated in this study (Fig. 2): a water tube representing a low atomic number material [Fig. 2(a)], a silicon tile representing a higher atomic number material [Fig. 2(b)], as well as an excised and fixated murine lung [Fig. 2(c)] to demonstrate generalizability of the water coefficients. The water tube was a 1.5 mL Eppendorf snap tube filled with tap water. The silicon ($Z = 14$) tile used was the lower portion of the axial spatial resolution module contained in a QRM micro-CT bar pattern phantom.²⁰ The dotted inset image of Fig. 2(b) shows the edge on view of the tile from the perspective of the detector. The spatial resolution module in the phantom is etched into the top 100 μm of a 500 μm thick silicon tile. However, for this study we used the remaining 400 μm thick un-etched silicon region to evaluate the performance of the proposed method in a sample generating more severe beam hardening artifacts. Finally, the murine lungs used were excised from an *ex vivo* sample. All animal studies were approved by Mayo Clinic's Institutional Animal Care and Use Committee. The lungs were surgically removed, cannulated, and instilled with a fixation solution of 50% PEG 400, 25% Ethyl alcohol, 10% formaldehyde, and 15% water to a filling pressure of a 20 cm water column. The lungs were tied off at the trachea and immersed in the same solution for 7 days before being air inflated at 25 mmHg and

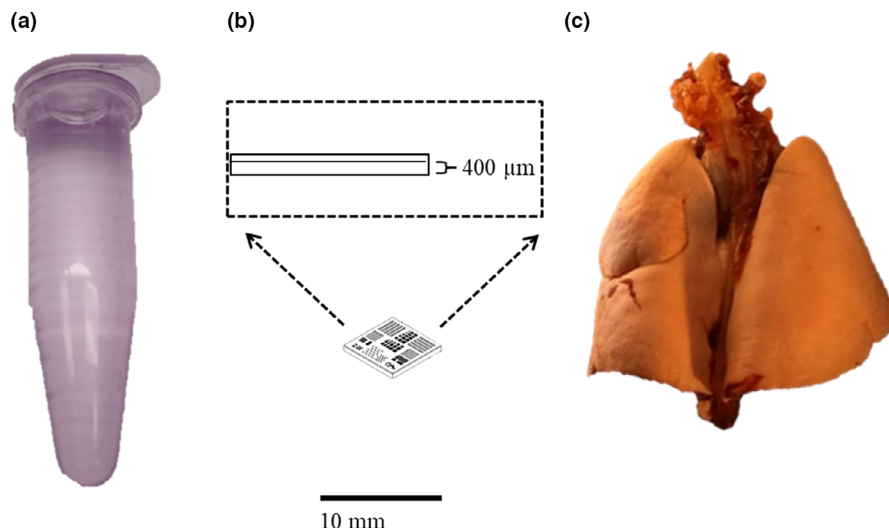


FIG. 2. Imaged samples shown to scale include (a) 1.5 mL snap tube filled with water, (b) QRM micro-CT bar pattern phantom schematic adapted from Ref. [20]. The inset shows an enlarged view of the chip and the edge-on orientation used to acquire images. The lower 400 μm silicon region was used exclusively in this study. (c) Posterior view of excised murine lung with heart following fixation and air drying at end-exhalation inflated volume. [Color figure can be viewed at wileyonlinelibrary.com]

dried for 72 h.²¹ The final product used for imaging is shown in Fig. 2(c). This fixation method preserves native air-tissue contrast as well as the inflated structure of the lung, and is a standard method for *ex vivo* structural imaging as determined by the American Thoracic Society guide on structural lung imaging.²²

2.C. Data acquisition and image reconstruction

The grating interferometer system used is shown schematically in Fig. 1(a) with gold Sunray design^{14,23} absorption gratings manufactured by Microworks GmbH (Karlsruhe, Germany). Further details about the source grating G_0 , the $\pi/2$ phase shift grating G_1 (design energy of 40 keV), and analyzer grating G_2 used in the study are listed in Table I.

All measurements in this investigation used a Talbot-Lau geometry at the first Talbot distance with a G_0 to G_1 distance of $d_{01} = 522$ mm and a G_1 to G_2 distance of $d_{12} = 251$ mm. All gratings were centered around the central beam with the grating rules aligned vertically parallel to the sample axis of rotation [z axis in Fig. 1(a)] and perpendicular to the lateral phase stepping direction. Mechanical phase stepping was performed along the x axis to sample the Talbot interference pattern using a nano-OP65 piezoelectric stage (Mad City Labs, Madison, WI, USA) underneath G_1 . X rays were generated from a Panalytical XRD source with a $400 \times 800 \mu\text{m}^2$ focal

spot size on a tungsten anode operated at 55 kVp and 40 mAs filtered with a 200 μm thick beryllium window. The source spectrum, simulated with SPEKTR,²⁴ is shown in Fig. 3. The detector used was a Princeton Instruments PIXIS 2048 CCD camera with an imaging area of 27.6×27.6 mm² and native 13.5 μm pixels binned 4 \times 4 and a 0.5 mm thick CsI:Tl single-crystal scintillator. The detector was placed directly behind G_2 covering a central square sub-region of the grating.

Sample and reference phase stepping curves (subscripted s and r , respectively) were generated by the phase stepping of G_1 over a single period of G_1 in six steps of 1.5 s each for a total of 9 s per view angle. Projection data of the three contrasts were then generated using one-dimensional Fast Fourier Transforms of the phase stepping curves acquired at each pixel.²⁵ Absorption contrast A was calculated as the negative log ratio of the sample and reference zeroth order Fourier coefficients of the phase stepping curves, denoted a_0 ,

$$A = -\ln\left(\frac{a_{0,s}}{a_{0,r}}\right). \quad (7)$$

Differential phase $\Delta\phi$ was calculated as the phase difference between the first Fourier coefficients,

$$\Delta\phi = \phi_{1,s} - \phi_{1,r}. \quad (8)$$

TABLE I. Grating specifications of the experimental Talbot-Lau system. The lamellae heights are design heights and vary across a grating due to imperfections.

Grating	Period (μm)	Duty cycle (%)	Lamellae material	Lamellae height (μm)	Size (cm ²)	Substrate material	Substrate thickness (μm)
G_0	10.0	55	Au	120	6 \times 6	graphite	500
G_1	3.24	55	Au	2.6	6 \times 6	Si	200
G_2	4.8	55	Au	120	6 \times 6	graphite	500

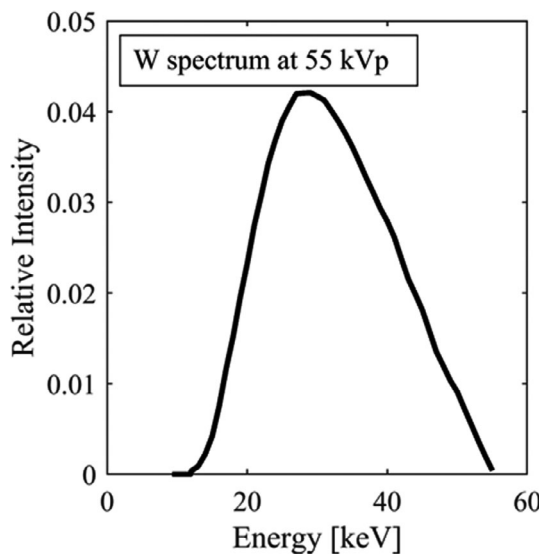


Fig. 3. Normalized source spectrum produced by a tungsten source operated at 55 kVp.

Integral phase ϕ was used for image reconstruction calculated by integrating the projection in the direction of phase stepping. Finally, visibility refers to the amplitude of the Talbot interference pattern relative to its baseline value, which for the reference phase stepping curve is calculated as $V_{1,r} = \frac{a_{1,r}}{a_{0,r}}$. We then define normalized visibility contrast V as the ratio of the sample and reference phase stepping curve visibilities,

$$V = \frac{V_{1,s}}{V_{1,r}} = \frac{a_{1,s} a_{0,r}}{a_{0,s} a_{1,r}}. \quad (9)$$

In our experimental setup mean reference visibility was measured to be $V_{1,r} = 16.4\%$. In our study, we assume the line integral of local visibility reductions through the sample to be proportional to $-\ln(V)$, which has been demonstrated for the small-angle-scatter component of normalized visibility.^{26,27} While there are factors other than small-angle scattering that contribute to visibility reduction, this assumption enables the use of coefficients fitted with reconstructed visibility calibration images to correct projections. Thus, in this work we define the visibility projections to include a negative log operation such that $q_V = -\ln(V)$.

Using the aforementioned phase stepping and retrieval procedure, water, silicon, and murine lung samples were positioned with a source-to-object distance of $d_{SO} = 710$ mm and object-to-detector distance of $d_{OD} = 110$ mm to perform CT [Fig. 1(a)]. All CT acquisitions were performed over a full 360 degree range such that any ring artifacts would be presented as full rings. Due to the rotational symmetry of the water cylinder projection data were acquired every 2 degrees, while projections of both the silicon tile and fixed lung were acquired every 0.5 degrees. Images were then reconstructed into 512×512 matrix slices of $47 \mu\text{m}$ isotropic voxels using the FDK algorithm²⁸ as implemented in the TIGRE reconstruction suite.²⁹ In order to minimize image noise when determining correction coefficients, both the water cylinder and silicon tile images

were reconstructed with TIGRE's Hamming filter while lung images were reconstructed with a Ram-Lak filter appropriate for the high frequency features in the lungs.

2.D. Empirical determination of normalized visibility spatial modulating term M_V

Previous evidence has shown polychromatic normalized visibility measurements to be influenced by both absorption and phase properties in a material- and system-dependent manner¹³ thus we sought to determine M_V from Eq. (5) using the system and samples described in Sections 2.B and 2.C. To this end, repeat projections of the water and silicon samples were averaged to obtain low noise projections showing grating-induced spectral artifacts for each contrast. This enabled low-noise comparisons of how artifacts in each contrast projection correlated with air scan grating projections. For each contrast, pixel patches from within the sample region of the low-noise projections were selected and compared against the corresponding air scan grating patches. Using these patches the Pearson correlation coefficient magnitude $|\rho|$ was calculated to evaluate how well each reference air scan patch [$a_{0,r}, \phi_{1,r}$, and $V_{1,r}$ from Eq. (7)–(9)] correlated with the grating-induced beam hardening artifacts in each sample projection patch. The correlation magnitude $|\rho|$ was used because the solution to the interpolation problem finds the proper sign. For a given sample material we determined that the spatial modulating term for a given contrast k should be the reference image r (where $r = a_{0,r}, V_{1,r}$, or $\phi_{1,r}$) that maximizes $|\rho|$ for a given contrast projection k , thus,

$$M_k = \operatorname{argmax}_r |\rho_{k,r}|. \quad (10)$$

This procedure was performed to determine the spatial modulating term for normalized visibility M_V in both water and silicon samples.

A similar approach to finding the spatial modulating terms M_k would be to solve Eq. (6) determining coefficients c_k for each contrast k and reference image r for M_k and selecting the combination that yields the best correction as determined by the criteria described in Section 2.5. We argue, however, that the above approach of using low-noise projections and comparing correlations yields the same results while requiring fewer image reconstructions. We confirm this approach by determining the normalized visibility modulating term M_V using both described methods.

An overview of the steps involved in EBHC-GI is given in Fig. 4 which includes the steps involved in calculating correction coefficients c_k as well as applying them in correcting polychromatic projections. In this study, we have implemented EBHC-GI assuming other system specific calibrations (e.g., traditional flat-field and dark-current corrections, center of rotation calculations, bad pixel corrections) have been performed on the polychromatic projections q_k and M_k . EBHC-GI models artifacts to have originated from the sample and the gratings, represented by q_k and M_k respectively.

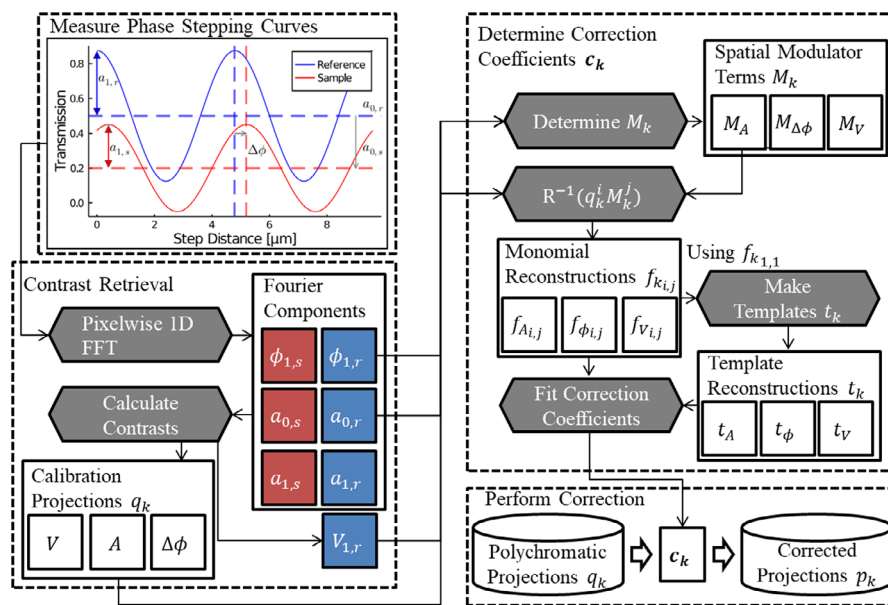


FIG. 4. Overview of processing steps involved in EBHC-GI. Three contrast calibration projections q_k retrieved from phase stepping curves acquired of a sample object with a known homogenous region are used to fit correction coefficients for each contrast c_k that are used to correct future projections of similar materials. [Color figure can be viewed at wileyonlinelibrary.com]

However, because EBHC-GI is an empirical linearization technique, other residual system defects or artifacts that remain in projections q_k and M_k , if they are stable and reproducible over the duration of a CT scan, also have potential to be corrected for with EBHC-GI.

2.E. Evaluation of EBHC-GI

After determining the grating term for normalized visibility M_V , sets of correction coefficients c_k were then calculated from the water sample and silicon sample image data as described by Eq. (6). These coefficients were then applied to the original projection data and reconstructed into axial images for subsequent analysis.

The performance of our correction was quantified in terms of a reduction in the mean squared error (MSE) defined by:

$$\text{MSE} = \frac{1}{n} \sum_i^n (e_i)^2, \quad (11)$$

where $e = P_k(\mathbf{r}) - t_k(\mathbf{r})$ is the n voxels difference image between the template image $t_k(\mathbf{r})$ and the corrected image $P_k = R^{-1}(p_k)$, which was reconstructed using EBHC-GI corrected projections p_k of Eq. (5). Standard deviation measured in a central homogenous region of each sample image was used as a secondary measure of artifact reduction. These values were then used to compare the uncorrected and corrected images for each contrast. Line profile comparisons were also performed to visually compare the uncorrected, corrected, and template images.

Finally to assess the generalizability of the coefficients to similar materials we concluded our investigation by applying the coefficients determined from the water sample on the murine lung sample. Performance was assessed qualitatively

for each contrast by visual inspection of uncorrected, corrected, and subtraction images.

3. RESULTS

3.A. Determining the spatial modulating term M_V for normalized visibility

The correlation of grating-induced artifacts between sample and grating projections is shown as a bar chart comparison in Fig. 5 for both water and silicon samples. The height of each bar indicates the magnitude of the Pearson correlation coefficient $|\rho|$. Stars indicate correlations that were significant, which was defined as having a $P < 0.05$. For a given contrast (e.g., absorption), the correlation of the sample projection against the reference projection for each contrast is depicted as a differently shaded bar (i.e., black, gray, or white for absorption, differential phase, and normalized visibility, respectively). For example the black bar in the group of three bars for absorption contrast refers to the correlation $|\rho_{A,a_{0,r}}|$.

From the results depicted in Fig. 5, we observed that the correlation of artifacts in the absorption contrast was highest with the absorption reference for both the water and silicon samples. Thus, for both water and silicon samples, from Eq. (10) we determined the absorption grating term to be $M_A = a_{0,r}$. A similar result was observed in both the water and silicon samples for differential phase contrast, namely that $M_{\Delta\phi} = \phi_{1,r}$, albeit the calculated phase correlations in the water sample were not significant due to the low correlation across all contrasts. This was consistent with our observation that artifacts were absent in the water differential phase projections, indicating a minimal $M_{\Delta\phi}$ contribution to the correction. For the normalized visibility contrast, we

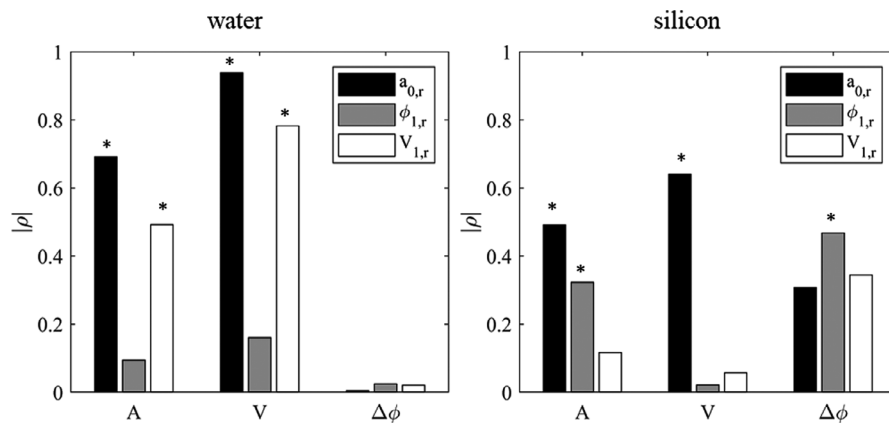


FIG. 5. Pearson correlation coefficient magnitudes $|\rho|$ between sample and air grating projections for both the water and silicon samples. *indicates a $P < 0.05$.

observed $|\rho_{V,a_0,r}| > |\rho_{V,V_1,r}|$ in both sample materials. This result suggests that $M_V = a_{0,r}$ and provides further evidence of cross-contamination of absorption and phase information into the visibility contrast, an effect previously reported in experimental studies.³⁰ The finding that $|\rho_{V,a_0,r}| > |\rho_{A,a_0,r}|$ is in part also a consequence of comparing correlations between fundamentally different contrast mechanisms. Visibility is an edge-enhancing contrast and outside of edge regions it better resembles an air scan, yielding a comparatively higher correlation score.

3.B. Evaluation of EBHC-GI in water

Using the M_k grating terms determined for water in Section 3.A, fit coefficients for the water sample were determined using the original and template images shown in Fig. 6. In the water sample, second degree polynomial coefficients were determined for both variable dimensions resulting in nine total coefficients for each contrast. The choice of second degree polynomials for the water sample was determined empirically to best remove spectral artifacts with no substantial improvement observed by adding higher polynomial terms.

Figure 7 then compares the resulting images reconstructed from uncorrected projections and EBHC-GI corrected projections. Line profile comparisons including the template image are included in Fig. 7(c). The measured MSE and standard deviation averaged over 30 central slices containing ring artifacts are presented in Table II. In all three contrasts there was little evidence of cupping artifacts suggesting a limited influence of beam hardening from the water tube due to its small size and lower atomic number. However, the presence of ring artifacts in the absorption contrast reflects the spectral nonuniformity from the gratings observed quantitatively as an elevated MSE and standard deviation reported in Table II. Of note, these ring artifacts are strongly suppressed following the application of EBHC-GI where the absorption MSE was decreased by 80% and standard deviation by 57%. In the normalized visibility channel, the influence of beam hardening is not obvious. Despite this, we measured a 65% reduction in the normalized visibility standard deviation following

correction using $M_V = a_{0,r}$ compared to only a 58% reduction using $M_V = V_{1,r}$ with comparable reductions in MSE in both cases.

The presented images and measured results are representative of typical slices in the reconstructed volume containing spectral ring artifacts. In EBHC-GI M_k controls the local ring artifact correction, and as a result slices containing rings experience a reduction in MSE and standard deviation following EBHC-GI correction, whereas slices without prominent rings are left largely unchanged. Similar observations were made in the differential phase contrast images where spectral artifacts were visually undetectable in the original images. Thus, the original and corrected images were indistinguishable with a correspondingly small reduction in MSE and standard deviation.

These results suggest that for our given system in water, the absorption contrast is most strongly influenced by beam hardening and, in this low-Z imaging task, benefits most from EBHC-GI in terms of ring artifact reduction, reduced MSE from the template, and reduced standard deviation. Additionally, the improvements observed in water for the absorption and visibility channels also suggest that beam hardening affects intensity-like features of the phase stepping curve [a_0 and a_1] from Eqs. (7), (9)] more than the phase term.

3.C. Evaluation in higher atomic number materials

Using correction coefficients c_k determined for silicon, image and line profile comparisons for each contrast from the original and corrected silicon sample projections are shown in Fig. 8 with MSE and standard deviation values reported in Table III. For the higher atomic number silicon sample, third degree polynomial coefficients were determined for each variable yielding 16 coefficients per contrast. The additional polynomial terms were found to further improve artifact reduction over the second degree polynomial used with the water sample. Such results are plausible given the higher atomic number of silicon and hence greater degree of beam hardening. In the silicon tile images, all contrasts presented more severe artifacts than in water, with rings in each contrast, cupping in phase, and capping in the normalized

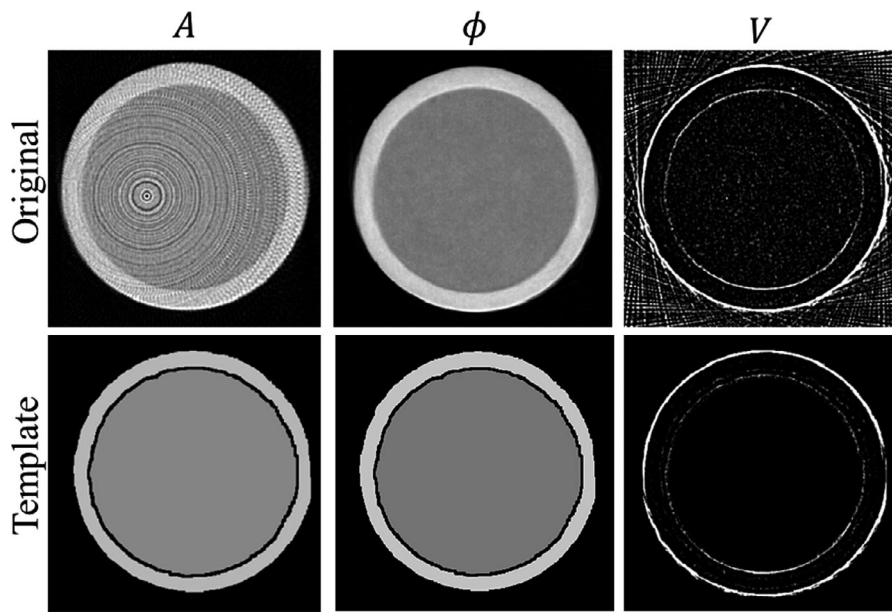


FIG. 6. Uncorrected reconstructions and artifact-free templates of the water sample for absorption A , phase ϕ , and normalized visibility V contrasts.

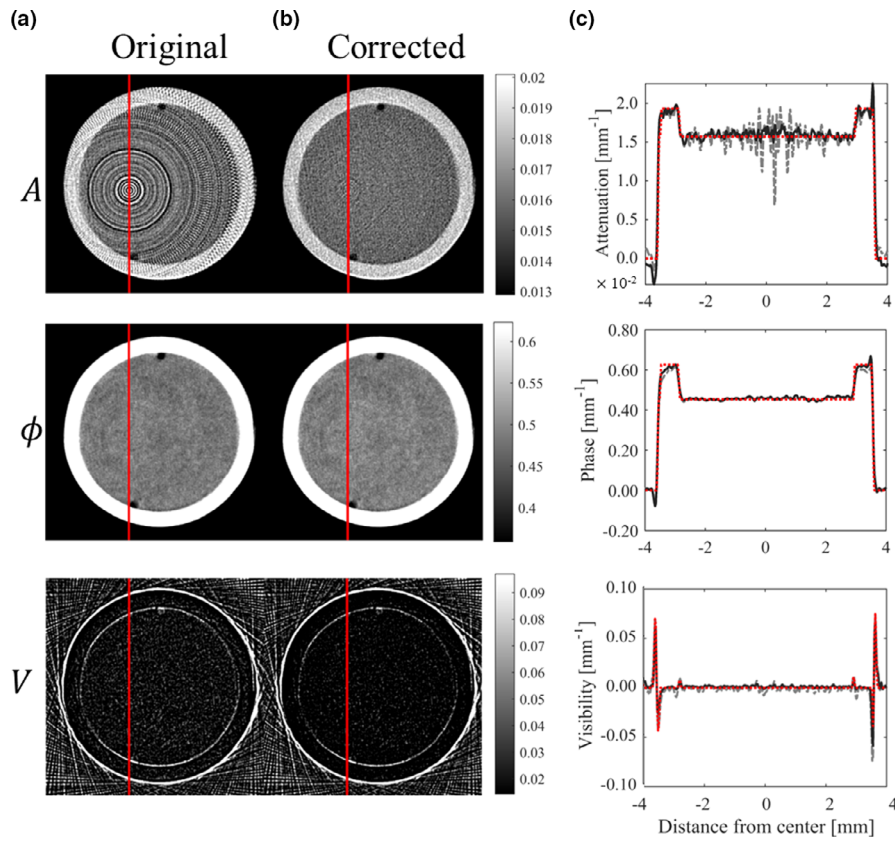


FIG. 7. Water sample reconstructions for each contrast with the original uncorrected axial image (a) shown left of the EBHC-GI corrected slice (b). The image display settings for each contrast are determined from the uncorrected image with a level equal to the image mean and window width of four standard deviations. (c) Line profiles that correspond to the columns of pixels marked in red in (a) and (b) compare original (dashed gray), corrected (solid black), and template (dotted red) line profiles. [Color figure can be viewed at wileyonlinelibrary.com]

visibility images. Furthermore, all three contrasts saw over 90% reductions in MSE following correction. These results are an improvement over using the visibility reference $V_{1,r}$

for M_V which resulted in only an 88.2% reduction in MSE and 40% reduction in standard deviation from the uncorrected image. Both values are less than the 90% and 51%

TABLE II. Beam hardening correction results for water quantified in terms of mean squared error (MSE) from template t and standard deviation (Std dev) within the homogenous water region.

Absorption			Phase			Visibility		
Image	MSE	Std dev	Image	MSE	Std dev	Image	MSE	Std dev
Original	1.33×10^{-6}	1.15×10^{-3}	Original	3.83×10^{-5}	6.02×10^{-3}	Original	7.58×10^{-6}	2.60×10^{-3}
Corrected	2.61×10^{-7}	4.85×10^{-4}	Corrected	3.63×10^{-5}	5.86×10^{-3}	Corrected	2.49×10^{-6}	8.86×10^{-4}
Change	-80.37%	-57.83%	Change	-5.22%	-2.66%	Change	-67.15%	-65.92%

reductions reported in Table III for visibility using $M_V = a_{0,r}$, confirming the conclusions from the correlation analysis presented for silicon in Fig. 5.

Compared to the reductions in MSE observed in the water sample following EBHC-GI, the reductions observed with the silicon sample were greater for all contrasts. This is in part due to the greater severity of spectral artifacts in the silicon sample but was also influenced by our use of MSE to quantify both ring and cupping artifacts. Ring artifact severity decreases sharply away from the image center while cupping severity does this to a lesser degree, which biased our results to have greater MSE for cupping over ring artifacts. In addition, despite having a greater reduction in MSE and standard deviation, we observed more residual ring artifacts in the silicon sample compared to the water sample. This was a consequence of the silicon sample inducing more beam hardening

and thus making the correction more challenging. Finally, the presence of spectral artifacts for all three contrasts in the silicon sample differs from our observations in the water sample, where spectral artifacts were primarily present for only the absorption and visibility contrasts. This suggests a material and contrast dependence for spectral artifacts.

3.D. Lung imaging application

The original and corrected images of the murine lung specimen are shown approximately midway through the mediastinum alongside difference images in Fig. 9. Similar to observations in the water sample, the most noticeable artifacts were the rings in the original absorption image, which were effectively eliminated in the corrected series. Examining the absorption difference images shows the rings removed

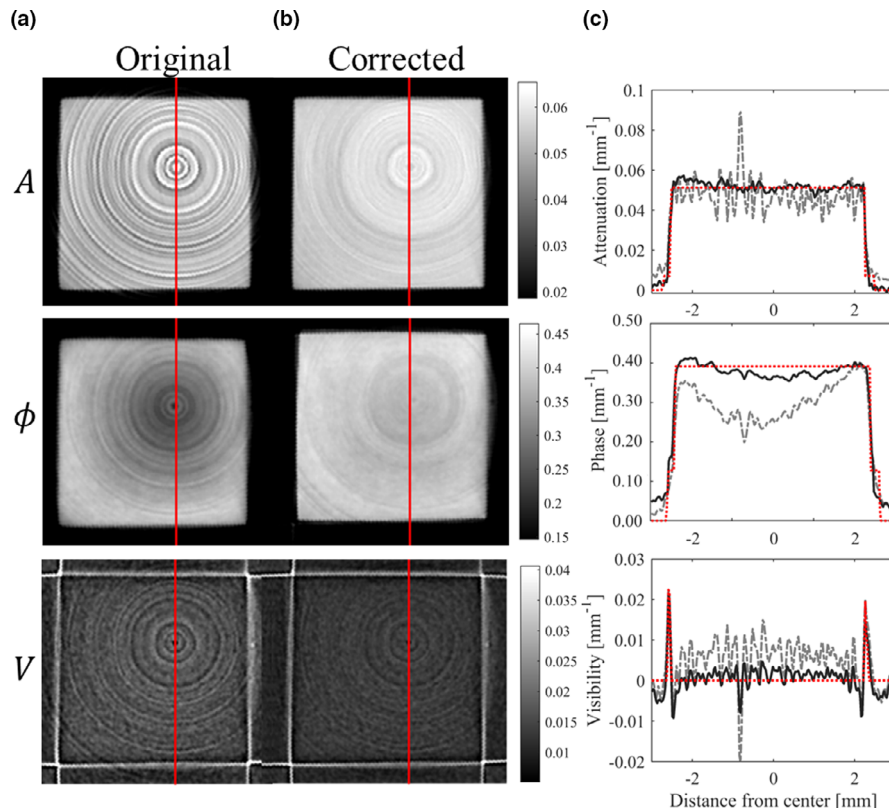


FIG. 8. Silicon tile reconstructions of attenuation, phase, and normalized visibility contrasts. Uncorrected images (a) are shown to the left of EBHC-GI corrected slices (b). The image display settings for each contrast are determined from the uncorrected image with a level equal to the image mean and window width of four standard deviations. (c) Line profiles that correspond to the columns of pixels marked in red in (a) and (b) compare original (dashed gray), corrected (solid black), and template (dotted red) line profiles. [Color figure can be viewed at wileyonlinelibrary.com]

TABLE III. Beam hardening correction results for silicon quantified in terms of MSE from the template and standard deviation of values within the homogenous silicon region.

Absorption			Phase			Visibility		
Image	MSE	Std dev	Image	MSE	Std dev	Image	MSE	Std dev
Original	6.76×10^{-5}	5.61×10^{-3}	Original	8.30×10^{-3}	3.62×10^{-2}	Original	5.15×10^{-5}	3.38×10^{-3}
Corrected	4.06×10^{-6}	1.94×10^{-3}	Corrected	2.67×10^{-4}	1.17×10^{-2}	Corrected	4.65×10^{-6}	1.65×10^{-3}
Change	-94%	-65.24%	Change	-96.78%	-67.68%	Change	-90.97%	-51.18%

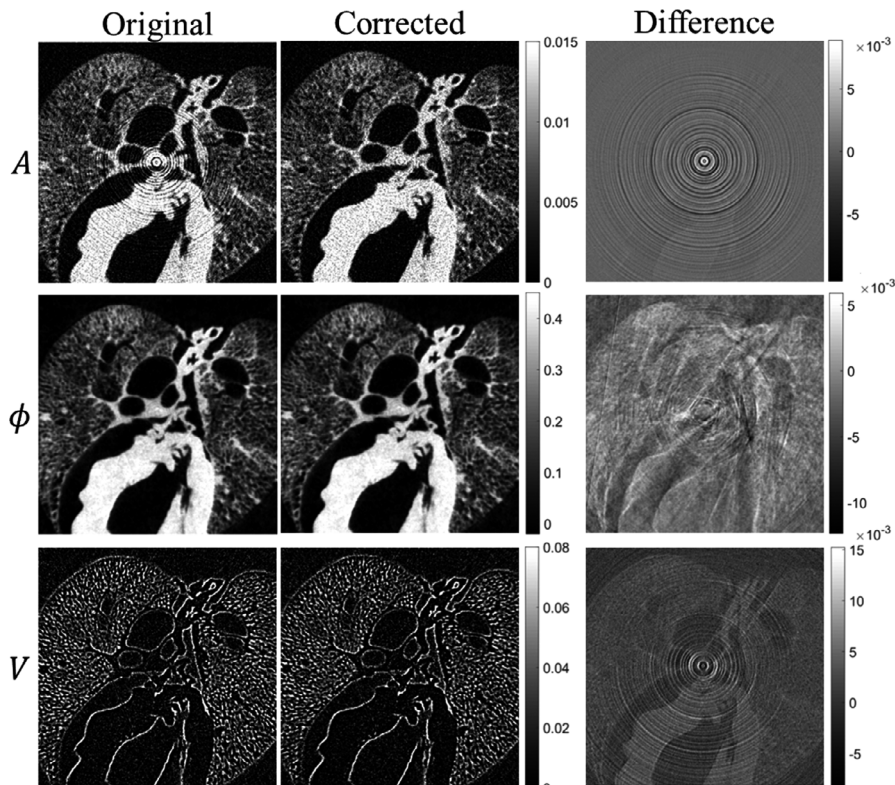


FIG. 9. Axial murine lung reconstructions in prone position show the heart, large airways, and lung parenchyma. Absorption, phase, and normalized visibility contrast images are shown both before and after corrections along with a difference image. The display settings are set equal for both corrected and uncorrected sets.

from the original with some faint residual anatomical features. These features were not lost in the corrected image, but their signal values were changed slightly, which is a consequence of EBHC-GI acting on materials different from the calibration material. However, given that materials in this murine sample are similar to water, these differences were small. In the corrected phase contrast images, there were no prominent rings in the uncorrected images and thus images are mostly unchanged following correction. The difference image does reveal subtle signal changes similar to those described for the water sample. While the image texture differs from the absorption difference image, this is because EBHC-GI is applied to differential phase contrast prior to the integration step and thus these local differences are spread out to some extent. In the normalized visibility images, there was evidence of removed rings as well as nonedge signal

changes in the difference image, which is again due to EBHC-GI subtly shifting signal values for materials not present in the calibration object. Together, our results in the murine lung sample were consistent with those seen in the water phantom, in particular, that the absorption contrast was most susceptible to grating induced ring artifacts, but that they could be readily removed using EBHC-GI.

4. DISCUSSION

The key findings from our study are that beam hardening artifacts in grating-based x-ray phase contrast imaging can be largely suppressed by applying a two-variable polynomial correction to each of the derived contrasts. Specifically, the two-variable approach includes both sample projections and grating projections in each contrast so as to correct for both

cupping and capping artifacts derived from beam hardening in the sample as well as spectral artifacts from the gratings. The changes made to the originally described ECCP¹⁸ included applying the polynomial correction separately for each contrast mechanism to account for the different energy dependencies of the different contrast mechanisms and using projections of the system gratings instead of a primary modulator. We also showed methods to best determine this grating term for normalized visibility contrast which is influenced by both the imaging system and sample.

In determining the grating term for normalized visibility contrast M_V using a correlation analysis with grating projections, we found for both materials studied that the normalized visibility sample projections had the highest correlation with the absorption grating projections. These results differ from directly extrapolating ECCP to each contrast, which would have suggested using the reference visibility image $V_{1,r}$. However, these observations of system and material dependencies of grating-induced artifact in the normalized visibility contrast are consistent with previous work that showed similar influence of absorption and phase information in polychromatic visibility measurements.¹³ In our particular investigations, including the broad spectrum used and materials studied, we found spectral artifacts in the absorption contrast to have greater influence in normalized visibility projections. The cross-contamination between the three contrast mechanisms that occurs due to beam hardening is but one of several sources of bias in normalized visibility imaging present in grating based laboratory setups.^{12,30–32} In order to perform better quantitative studies²⁷ of the small-angle scattering and sub-resolvable structural information contained in the visibility signal, these systematic influences must be understood and accounted for. A limitation of our method in this regard is its empirical approach to generating the visibility template image. Assigning known homogenous regions in our test objects to have a normalized visibility signal equivalent to air was necessary as it was unclear as to what would make an ideal visibility calibration object. This is coupled with the fact that the choice of an ideal normalized visibility test object would likely be specific to material, energy and other systemic factors.³⁰

After determining the grating terms M_k and applying our found fit coefficients for each contrast and material, our results demonstrated the benefit of applying a unique set of correction coefficients for each contrast. We saw this in varying contributions of cupping and ring artifacts between materials and contrasts. The uncorrected water absorption image suffered most from grating-induced ring artifacts and needed a strong correction, whereas the phase image required minimal correction. In the silicon tile we observed an even greater divergence of artifacts between the three contrasts. The silicon absorption image presented severe ring artifacts with modest cupping, while the phase image had more severe cupping. Finally, the silicon visibility image had modest capping and rings. In both samples studied, these results suggest a material and contrast dependence on the observed spectral

artifacts. This dependence is consistent with previous findings.^{9,11}

Like ECCP, our proposed method, EBHC-GI, is a first-order correction and thus some rings remained due to detector gain inconsistencies or higher order beam hardening effects. Removing these residual artifacts would be best handled with iterative methods¹⁰ adapted to account for spatially varying grating effects or additional image filtering.³³ Additionally for the normalized visibility contrast, improved artifact reduction may be possible by first separating the influences of other contrasts.¹³ Another approach would be to add a second modulating term to include both visibility and absorption. However, this comes at the cost of increasing the number of images required to determine the correction coefficients.

We then demonstrated the generalizability of correction coefficients derived using one material with a similar atomic number. Our water correction coefficients produced similar ring artifact removal in a murine lung sample as they did in a water sample. A limitation of our lung sample preparation was that the ribcage and other natural boney anatomy surrounding the lungs were not retained following excision for fixation. Thus our lung image results do not show the typical shadowing that occur around bone as a result of beam hardening. While a prereconstruction linearization technique calibrated with a water sample would partially compensate for this shadowing, if the materials to be imaged were known ahead of time, those materials could be included in the calibration phantom to increase the effective range of materials to be corrected. For imaging objects with large proportions of both low and high atomic number materials, say largely boney anatomy, a multistep approach may be required. Postreconstruction iterative techniques^{34–36} could be utilized to further improve spectral artifact compensation in these multimaterial situations. Ultimately, the choice of spectral compensation technique is highly application dependent. Nonetheless, our proposed EBHC-GI method could readily be implemented as one step in the x-ray grating interferometry image processing pipeline.

Finally, the push to enable human imaging with grating interferometry^{37–39} requires higher x-ray energies (e.g., high tube potential settings) and larger fields-of-view which places even higher demands on grating design and fabrication. Because partial transmission becomes unavoidable in these circumstances, and even desirable in others,^{14,40,41} our results demonstrate that image quality can be preserved for all three contrast mechanisms using a polychromatic x-ray source. This eases the requirements for grating design and fabrication and may facilitate multicontrast x-ray studies in humans.

5. CONCLUSIONS

In this investigation we introduced an empirical correction for beam hardening in grating interferometry, EBHC-GI, that is an extension of a two-variable polynomial correction for primary modulators that we adapted to the unique contrast mechanisms and system properties of a grating

interferometer. These adaptations included applying the polynomial correction to each contrast mechanism separately and determining an optimal spatial modulating term for the normalized visibility contrast. In absorption and phase contrast images, this term was the reference projection data for each respective contrast mechanism. However, due to cross-contamination of absorption and phase contrast information into the visibility channel, the optimal visibility modulating term was determined for our system to be the absorption reference projection data. Quantitative assessment of our method showed a reduction in beam hardening artifacts due to both the sample and the gratings in both water and silicon test objects, representing imaging of low and high atomic number materials, respectively. This empirical method can be used, without the need of detailed system or sample knowledge, to correct for beam hardening effects in the sample and in the gratings. Once determined, the coefficients can be used on all subsequent scans of like materials performed with similar acquisition settings.

ACKNOWLEDGMENTS

The authors thank Jeffrey Meridew, Nunzia Caporarello Ph.D., and Daniel Tschumperlin Ph.D. for their help in providing the murine sample used and Andrea Bracchetti for his help in performing the fixation. We also thank Marcus Zuber, Sabine Bremer, and the other members of the Laboratory for Applications of Synchrotron Radiation (LAS) at the Karlsruhe Institute for Technology for their help in testing the quality of our gratings. This work was funded by Mayo Clinic ASU Team Science Award and supported in part by the Mayo Clinic X-ray Imaging Research Core. We acknowledge the support of the CT Clinical Innovation Center and the Mayo Clinic Graduate School of Biomedical Sciences.

CONFLICT OF INTEREST

Research support is provided to the Mayo Clinic from Siemens Medical Solutions, USA, unrelated to this work. At the time of publication, Dr. Shanblatt is an employee of Siemens Healthcare. Thomas Koenig is an employee of Ziehm Imaging. The remaining authors have no relevant conflict of interest to disclose.

^aAuthor to whom correspondence should be addressed. Electronic mail: nelson.brandon@mayo.edu.

REFERENCES

1. Donath T, Pfeiffer F, Bunk O, et al. Toward clinical X-ray phase-contrast CT: demonstration of enhanced soft-tissue contrast in human specimen. *Invest Radiol*. 2010;45:445–452.
2. Bech M, Jensen TH, Feidenhans'l R, Bunk O, David C, Pfeiffer F. Soft-tissue phase-contrast tomography with an x-ray tube source. *Phys Med Biol*. 2009;54:2747–2753.
3. Momose A, Takeda T, Itai Y, Hirano K. Phase-contrast X-ray computed tomography for observing biological soft tissues. *Nat Med*. 1996;2:473–475.
4. Pfeiffer F, Weitkamp T, Bunk O, David C. Phase retrieval and differential phase-contrast imaging with low-brilliance X-ray sources. *Nat Phys*. 2006;2:258–261.
5. Bravin A, Coan P, Suortti P. X-ray phase-contrast imaging: from pre-clinical applications towards clinics. *Phys Med Biol*. 2013;58:R1–R35.
6. Brooks RA, Di Chiro G. Beam hardening in x-ray reconstructive tomography. *Phys Med Biol*. 1976;21:390–398.
7. Attwood DT, Sakdinawat A, Geniesse L. *X-rays and Extreme Ultraviolet Radiation: Principles and Applications*, Second edition. Cambridge, United Kingdom; New York, NY: Cambridge University Press; 2016.
8. Engelhardt M, Kottler C, Bunk O, et al. The fractional Talbot effect in differential x-ray phase-contrast imaging for extended and polychromatic x-ray sources. *J Microsc-Oxford*. 2008;232:145–157.
9. Munro PRT, Olivo A. X-ray phase-contrast imaging with polychromatic sources and the concept of effective energy. *Phys Rev A*. 2013;87:053838.
10. Yan AM, Wu XZ, Liu H. Beam hardening correction in polychromatic x-ray grating interferometry. *Opt Express*. 2017;25:24690–24704.
11. Chabior M, Donath T, David C, et al. Beam hardening effects in grating-based x-ray phase-contrast imaging. *Med Phys*. 2011;38:1189–1195.
12. Yashiro W, Vagovic P, Momose A. Effect of beam hardening on a visibility-contrast image obtained by X-ray grating interferometry. *Opt Express*. 2015;23:23462–23471.
13. Pelzer G, Anton G, Horn F, et al. A beam hardening and dispersion correction for x-ray dark-field radiography. *Med Phys*. 2016;43:2774–2779.
14. Trimborn B, Meyer P, Kunka D, et al. Imaging properties of high aspect ratio absorption gratings for use in preclinical x-ray grating interferometry. *Phys Med Biol*. 2016;61:527–541.
15. Gao H, Zhang L, Grimmer R, Fahrig R. Physics-based spectral compensation algorithm for x-ray CT with primary modulator. *Phys Med Biol*. 2019;64:125006.
16. Pfeiffer F, Bech M, Bunk O, et al. Hard-X-ray dark-field imaging using a grating interferometer. *Nat Mater*. 2008;7:134–137.
17. Kachelriess M, Sourbelle K, Kalender WA. Empirical cupping correction: a first-order raw data pre-correction for cone-beam computed tomography. *Med Phys*. 2006;33:1269–1274.
18. Grimmer R, Fahrig R, Hinshaw W, Gao H, Kachelriess M. Empirical cupping correction for CT scanners with primary modulation (ECCP). *Med Phys*. 2012;39:825–831.
19. Otsu N. Threshold selection method from gray-level histograms. *IEEE Trans Syst Man Cyb*. 1979;9:62–66.
20. Langner O, Karolczak M, Rattman G, Kalender WA. Bar and Point Test Patterns Generated by Dry-Etching for Measurement of High Spatial Resolution in Micro-CT. Paper presented at: World Congress on Medical Physics and Biomedical Engineering 2009; Munich, Germany.
21. Groskin SA, Heitzman ER. *Heitzman's the Lung, Radiologic-Pathologic Correlations*, 3rd edn. St. Louis: Mosby; 1993.
22. Hsia CCW, Hyde DM, Ochs M, Weibel ER. An Official Research Policy Statement of the American Thoracic Society/European Respiratory Society: standards for quantitative assessment of lung structure. *Am J Respir Crit Care Med*. 2010;181:394–418.
23. Jürgen Mohr TG, Kunka D, Johannes Kenntner J, Leuthold JM, Schulz J, Walter M. High aspect ratio gratings for X-ray phase contrast imaging. Paper presented at: International Workshop on X-ray and Neutron Phase Imaging with Gratings 2012; Institute of Multidisciplinary Research for Advanced Materials.
24. Punnoose J, Xu J, Sisniega A, Zbijewski W, Siewerssen JH. Technical note: spektr 3.0-A computational tool for x-ray spectrum modeling and analysis. *Med Phys*. 2016;43:4711.
25. Weitkamp T, Diaz A, David C, et al. X-ray phase imaging with a grating interferometer. *Opt Express*. 2005;13:6296–6304.
26. Chen GH, Bevins N, Zambelli J, Qi Z. Small-angle scattering computed tomography (SAS-CT) using a Talbot-Lau interferometer and a rotating anode x-ray tube: theory and experiments. *Opt Express*. 2010;18:12960–12970.
27. Bech M, Bunk O, Donath T, Feidenhans'l R, David C, Pfeiffer F. Quantitative x-ray dark-field computed tomography. *Phys Med Biol*. 2010;55:5529–5539.
28. Feldkamp LA, Davis LC, Kress JW. Practical cone-beam algorithm. *J Opt Soc Am A*. 1984;1:612–619.

29. Biguri A, Dosanjh M, Hancock S, Soleimani M. TIGRE: a MATLAB-GPU toolbox for CBCT image reconstruction. *Biomed Phys Eng Expr.* 2016;2:055010.
30. Koenig T, Zuber M, Trimborn B, et al. On the origin and nature of the grating interferometric dark-field contrast obtained with low-brilliance x-ray sources. *Phys Med Biol.* 2016;61:3427–3442.
31. Yashiro W, Noda D, Kajiwara K. Effect of insufficient temporal coherence on visibility contrast in X-ray grating interferometry. *Opt Express.* 2018;26:1012–1027.
32. Yashiro W, Momose A. Effects of unresolvable edges in grating-based X-ray differential phase imaging. *Opt Express.* 2015;23:9233–9251.
33. Munch B, Trtik P, Marone F, Stampanoni M. Stripe and ring artifact removal with combined wavelet–Fourier filtering. *Opt Express.* 2009;17:8567–8591.
34. Luo S, Wu H, Sun Y, Li J, Li G, Gu N. A fast beam hardening correction method incorporated in a filtered back-projection based MAP algorithm. *Phys Med Biol.* 2017;62:1810–1830.
35. Hsieh J, Molthen RC, Dawson CA, Johnson RH. An iterative approach to the beam hardening correction in cone beam CT. *Med Phys.* 2000;27:23–29.
36. Joseph PM, Spital RD. A method for correcting bone induced artifacts in computed tomography scanners. *J Comput Assist Tomogr.* 1978;2:100–108.
37. Willer K, Fingerle AA, Gromann LB, et al. X-ray dark-field imaging of the human lung-A feasibility study on a deceased body. *PLoS One.* 2018;13:e0204565.
38. Horn F, Leghissa M, Kaepller S, et al. Implementation of a Talbot-Lau interferometer in a clinical-like c-arm setup: a feasibility study. *Sci Rep.* 2018;8:2325.
39. Hauke C, Bartl P, Leghissa M, et al. A preclinical Talbot-Lau prototype for x-ray dark-field imaging of human-sized objects. *Med Phys.* 2018;45:2565–2571.
40. Wang ZT, Hauser N, Kubik-Huch RA, D'Isidoro F, Stampanoni M. Quantitative volumetric breast density estimation using phase contrast mammography. *Phys Med Biol.* 2015;60:4123–4135.
41. Meinel FG, Schwab F, Schleede S, et al. Diagnosing and mapping pulmonary emphysema on X-ray projection images: incremental value of grating-based X-ray dark-field imaging. *PLoS One.* 2013;8:e59526.